International Journal of Precision Engineering and Manufacturing-Green Technology
https://doi.org/10.1007/s40684-019-00061-0

Online ISSN 2198-0810
Print ISSN 2288-6206

REGULAR PAPER

Quantification of the Energy Flows During Ultrasonic Wire Bonding Under Different Process Parameters

Yangyang Long[1] · Friedrich Schneider[2] · Chun Li[1] · Jörg Hermsdorf[2] · Jens Twiefel[1] · Jörg Wallaschek[1]

Received: 26 March 2018 / Revised: 14 July 2018 / Accepted: 23 July 2018

Abstract

Despite of its wide and long-term application for interconnections in the field of microelectronics packaging, a quantitative understanding on the mechanisms of ultrasonic (US) wire bonding is still lacked. In this work, the energy flows from the electrical input energy to the different mechanisms during the US bonding process are quantified based on real-time observations via which the relative motions at the wire/substrate and the wire/tool interfaces can be detected. The relative motions at the two interfaces are proved to be caused by both the continuous plastic deformation and the US vibration. The normal force and US power interdependently affect the relative motion amplitudes. The deduced energy flows show that the energy from the transducer mainly flows to the vibration induced friction at the two interfaces and the microwelds formation, deformation and breakage. Despite of their significance to the process, the other mechanisms receive only little amount of energy. The impacts of the process parameters including normal force, US power and time on the energy flows are quantitatively investigated. A good coupling of the normal force and the US power guides more energy to the formation of microwelds while a long process time would increase the friction induced energy consumption.

Keywords Ultrasonic wire bonding · Relative motion · Energy flows · Process parameters · Interface

List of Symbols

F_N	The normal force
$F_{add,N}$	The additional normal force to deform the wire
u	The instantaneous voltage
i	The instantaneous current
t	Process time
R_m	The resistance of the transducer
C_m	The capacitance of the transducer
L_m	The inductance of the transducer
R_{VCA}	The resistance of the voice coil actuator
W_{NF}	The work conducted by the normal force
S_N	The tool tip displacement at the vertical direction
D_v	The vibration induced relative motion distance at horizontal direction
S_p	The plastic deformation induced relative motion displacement at horizontal direction
μ	The friction coefficient
μ_{mw}	The equivalent friction coefficient for microwelds formation, deformation and breakage
m	The mass of the wire underneath the tool tip
v_w	The vibration speed of the wire
φ	The cleaning coefficient
$E_{tran\ loss}$	The electrical loss energy to the transducer
$E_{storage}$	The storage energy of the transducer
$E_{tran\ input}$	The electrical input energy to the transducer
$E_{VCA\ loss}$	The loss energy from the voice coil actuator
$E_{VCA\ output}$	The output energy from the voice coil actuator
$E_{v\ friction}$	The vibration induced friction energy
$E_{p\ friction}$	The plastic deformation induced friction energy
$E_{v,\ wire}$	The kinetic energy for wire vibration
$W_{defor,\ wire}$	The work to deform the wire with additional force
$E_{NF\ defor,\ wire}$	The VCA energy for wire deformation
$E_{add\ p\ friction}$	The additional friction energy caused by the additional large normal force

✉ Yangyang Long
long@ids.uni-hannover.de

[1] Institute of Dynamics and Vibration Research, Leibniz Universität Hannover, Appelstr. 11, 30167 Hannover, Germany

[2] Laser Zentrum Hannover e.V., Hollerithallee 8, 30419 Hannover, Germany

Published online: 04 March 2019

$E_{v\ mw}$	The vibration induced energy for microwelds formation, deformation and breakage
$E_{p\ mw}$	The plastic deformation induced energy for microwelds formation, deformation and breakage
$E_{envi\ loss}$	The energy emitted to the environment

1 Introduction

Ultrasonic (US) wire bonding implements a normal force and US vibration (see Fig. 1) on a wire within a short period to create a bond between the wire and the substrate. Ever since its innovation in the 1960s, it has been the dominating interconnection technique in the microelectronics packaging industry [1, 2]. Since this technique was discovered by accident without knowing the mechanisms, much research has been conducted afterwards to reveal the bonding mechanisms [3, 4]. Nevertheless, a complete understanding on the mechanisms is still lacked, especially from a quantitative point of view, which is due to the short process time, the enclosed thin interfaces, the complex phenomena and the highly dynamic changes at the interfaces.

A fundamental issue among the unknown mechanisms is the relative motion behaviors at the interfaces. Within the bonding domain between the tool and the substrate as shown in Fig. 1, there are two interfaces—the wire/substrate (w/s) interface and the wire/tool (w/t) interface. As the bond is formed at the w/s interface, it is always the focus of research in this field. There is no doubt that the continuous plastic deformation causes a relative motion while the existence of the vibration induced relative motion at this interface has a

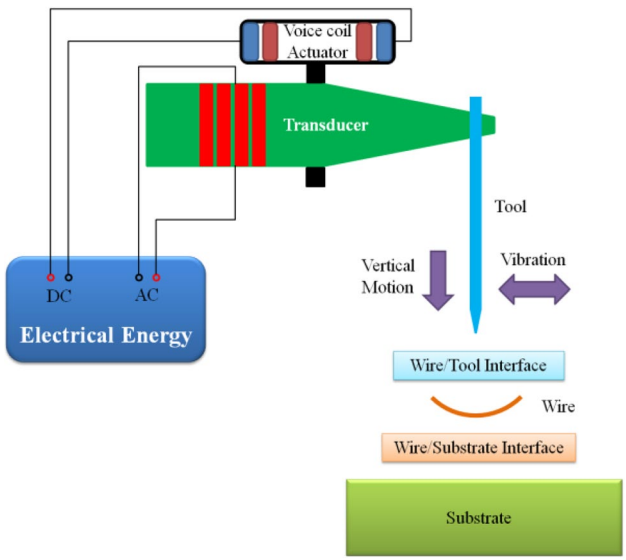

Fig. 1 Illustration of the bonding head and the bonding domain

long history of debate. In the beginning, some researchers considered that the friction induced thermal energy was profound at this interface [5]. With successful bonds in liquid nitrogen and the laser interferometer measurements, Joshi argued that no vibration induced relative motion occurred [6]. Winchell and Berg detected periodic groove structures on the silicon substrate, which can be a hint on the existence of the vibration induced relative motion [7]. Based on the laser vibrometer measurements, Osterwald found a difference between the vibration amplitudes of the wire and the pad [8]. In 2009, Gaul et al. captured the vibration induced relative motion at the bonding interface by using a high-speed camera [9]. According to Long et al., the relative motion behavior at this interface can be described by a combination of the Mindlin model and the stick–slip model [4].

Compared to the w/s interface, much less work has been conducted on the w/t interface which also plays an important role during the bonding process. The existence of a vibration induced relative motion at this interface was first discovered by Mayer et al. according to the analysis of the fifth harmonic of the stress signal [10]. No relative motion was observed in the high-speed video taken by Gaul et al. where transmitted light was used [11]. In contrast, the accumulation of the wire material on the tool, the wear of the wire and the wear of the tool indicated the occurrence of a relative motion [12–14]. In 2015, the relative motion was captured in the high-speed videos of thick aluminum wire and thick copper wire bonding [15, 16]. Later on, the relative motion was also detected by laser vibrometers [17]. It was also shown that the relative motion amplitudes at different locations of the interface are different, which indicated a similar relative motion behavior as that at the w/s interface [12].

Apart from the relative motions which cause the temperature increment and oxide removal [18], the wire vibrates and plastically deforms and microwelds form, deform and break. It is easy to understand the vibration of the wire as it is one of the purposes of the ultrasonic excitation. The continuous plastic deformation of the wire is due to the Acoustoplastic Effect (APE), which consists of stress superposition and acoustic softening [19]. According to the theory of Blaha and Lanenecker, the acoustic waves are preferably absorbed by the defects within crystals and the defects are then pushed away from their pinned positions [20]. The yield stress of the material is therefore significantly lowered and the wire can be further plastically deformed under the same normal force. Under the normal and tangential stress as well as the softening effect, the asperities on the metal surfaces deform as well. As the asperities get flattened and atoms from the surfaces of the bonding partners get closer and closer, microwelds can be formed. The deformation of asperities was also stated as the most important factor for bonding [21]. Along with the relative motion at the w/s interface, microwelds are deformed or even broken while new microwelds can

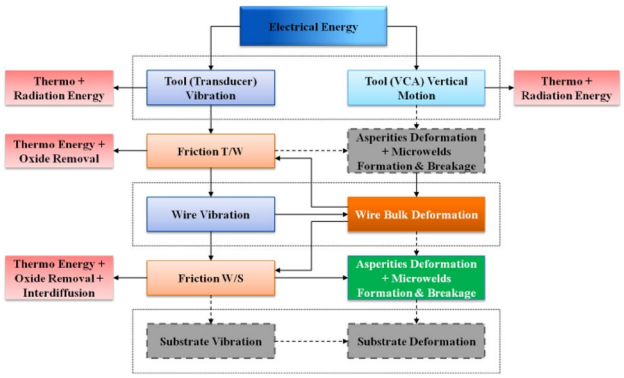

Fig. 2 The energy flows during the US wire bonding process

be simultaneously formed [4, 22, 23]. Once a microweld is formed, interdiffusion starts.

To make the explanation of the bonding process more concise and to make the quantitative investigation on the bonding process possible, an energy flow chart which is corresponding to the bonding domain in Fig. 1 is drawn in Fig. 2. The electrical energy from the power supply first flows to the main components of the bonding head—an US transducer and a voice coil actuator (VCA) which activate the vibration and the vertical motion of the bonding tool, respectively. Much energy is lost and converted to thermo and radiation energy during the transmission due to the impedance of the transducer and the VCA.

The energy is then transferred to the w/t interface. As described above, a relative motion exists at this interface and is caused by both the vibration and the plastic deformation (wire bulk deformation). The resulted friction consumes certain amount of energy. Some of the energy is converted to thermo energy and some is used for the oxide removal. In addition, both the friction and the vertical motion cause the deformation of asperities and the microwelds formation, deformation and breakage. Since this is not the bonding interface and the connection is very weak, this item can be ignored for simplification. The remained energy continues to pass through the wire and causes the vibration and the bulk deformation of the wire. The rest of the energy flows to the w/s interface. The functionalities of the energy at this interface are similar to those at the w/t interface but more prominent. Furthermore, interdiffusion takes place at this interface and would consume additional amount of energy. The substrate absorbs a certain amount of energy for its vibration and deformation. Since the vibration and deformation of the substrate is much smaller than those of the wire, this item can be ignored as well. Some energy could also be emitted to and dissipated in the ambient environment.

In this work, a quantitative understanding of the bonding process was obtained by quantifying the energy flows based on the real-time observation of the motions of the wire and the tool. In the following sections, the materials and experimental setup will be first described; the impacts of the process parameters including normal force, US power and time on the relative motion behaviors at the two interfaces are then discussed; finally, the calculations of the energy flows and their variations under different process parameter settings are provided in details.

2 Experiment

2.1 US Wire Bonding Setup

The aluminum wire used in this work is Al-H11 purchased from Heraeus GmbH. The diameter of the thick wire is 400 μm and it has a breaking load of 500–700 cN with more than 5% elongation. The thick aluminum wire bonding head HBK05 as shown in Fig. 3 was provided by Hesse Mechatronics GmbH. The natural frequency of the US transducer in the bonding head is around 60 kHz and was driven by an in-house developed digital phase controller [24] and a B&K 2713 amplifier.

2.2 Real-Time Observation System

The relative motion behaviors at the two interfaces were observed by a real-time observation system consisting of a high-speed camera and a magnification system as shown in Fig. 3. A Phantom v710 high-speed camera was used in this work. The pixels on the CMOS sensor of the camera have a size of 20 × 20 μm. Since the vibration amplitude of the tool tip is only a few microns for thick wire bonding, the camera itself is unable to capture the motion of the tool and the wire and a magnification system was thus integrated. In this work, a reverse lens technique was applied to enhance the resolution. The essential component of the technique is the reversed lens. With the selection of a C-Mount 12.5 mm Pentax lens which was connected to the black bellow (as shown in Fig. 3), a magnification of 18 × was obtained

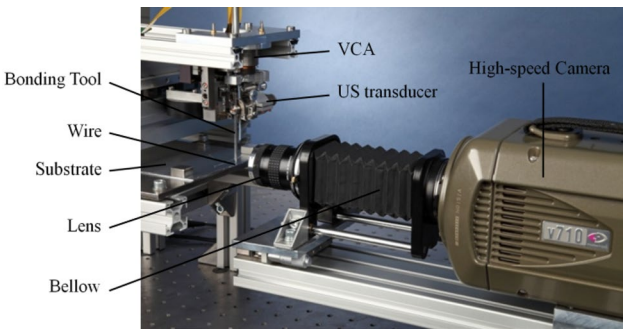

Fig. 3 Experimental setup for real-time observation of the bonding interfaces

for this system. Finally, a resolution of 1.1 µm/pixel was reached and the motions were able to be captured. Since the data writing speed of the camera is limited, a trade-off between the window size and the frame rate has to be made for recording the bonding process. Due to the continuous plastic deformation, the w/t interface is moving downwards during the bonding process. To keep the w/t interface inside the record window, a window size of 512 × 384 pixel was used and the record window is represented by the red rectangular in Fig. 4. With this window size, the highest frame rate that can be obtained is 30,008 fps. Even though the frame rate was smaller than the bonding frequency, the videos were able to record the relative motion behaviors because of the phase difference. The sharpness of the videos was assured by an exposure time of 2 µs.

To provide enough light onto the bonding site (563.2 × 422.4 µm) within the extremely short exposure time, a laser source JOLD-45-CPXF-1P was applied. The laser has a max power of 45 W and a wavelength of 804–808 nm depending on the applied power and temperature. The energy density of the laser beam on the wire was around 200 mW/mm^2. The influence of the laser radiation on the bonding process can be justified by the temperature increment induced by the laser beam. If the injection area on the wire is considered to be 400 × 400 µm and no heat transfer among the tool, wire and substrate occurs, the laser radiation induced temperature increment during 50 ms is only 7.38 K. In reality, the injection area is much smaller than 160,000 µm^2 and the metals have high heat transfer rates. As a result, the laser radiation has an insignificant influence on the bonding process.

2.3 Process Parameters

There are three process parameters that can significantly influence the bonding process as well as the energy flows. These are normal force, US power and process time. To study the impacts of the normal force and the US power, the two factors were varied at three different levels. Since the bonding processes were controlled by a phase-locked loop control, the driving powers were not the same as the set values. The exact values of the applied power consumptions were measured and shown in Table 1. The normal force can be accurately controlled as the same values in the table. Since the measurement tool used in this work is real-time observation, the impact of the time is always included. Therefore, all the processes were run and recorded for the same period of 50 ms.

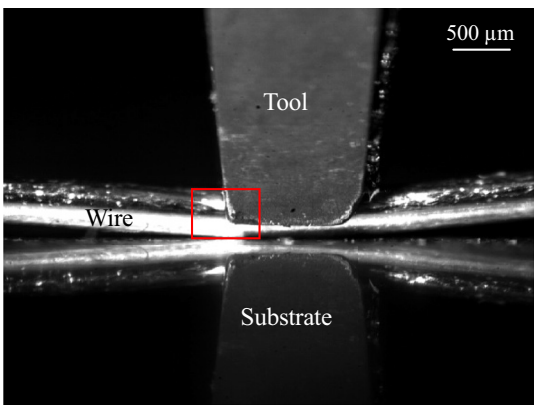

Fig. 4 Record window within the bonding domain

3 Results and Discussion on Real-Time Observations

3.1 Real-Time Observation

The bonding processes under different settings were recorded by the real-time observation system. The relative motions caused by both the continuous plastic deformation and US vibration were captured for all the processes. A bonding process under 9 N 24.8 W is shown in Figs. 5 and 6 to demonstrate the relative motion induced by continuous plastic deformation and US vibration, correspondingly. In Fig. 5, three images at the beginning, the middle and the end of the process were subtracted from the video and show a clear plastic deformation of the wire. The green curve in Fig. 5a represents the boundary between the wire and the tool while the w/s interface is represented by the blue line. Compared to the red circled area in Fig. 5a, some part of the wire that contacted the tool left filet was exposed in Fig. 5b. The plastic deformation continued and finally a larger region of the filet contacted part was exposed in Fig. 5c. The relative motion between the tool and the wire can be directly

Table 1 Applied US power of three levels under different forces

Normal Force \ US Power	Low	Medium	High
6 N	13.5 W	16.9 W	21.6 W
7.5 N	13.2 W	17.9 W	21.1 W
9 N	12.7 W	15.8 W	24.8 W

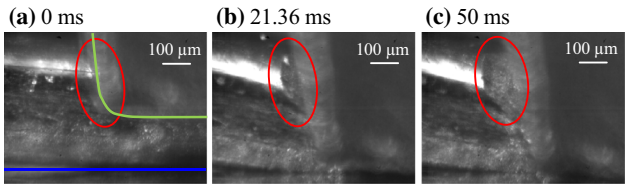

Fig. 5 Continuous plastic deformation induced relative motion under 9 N 24.8 W

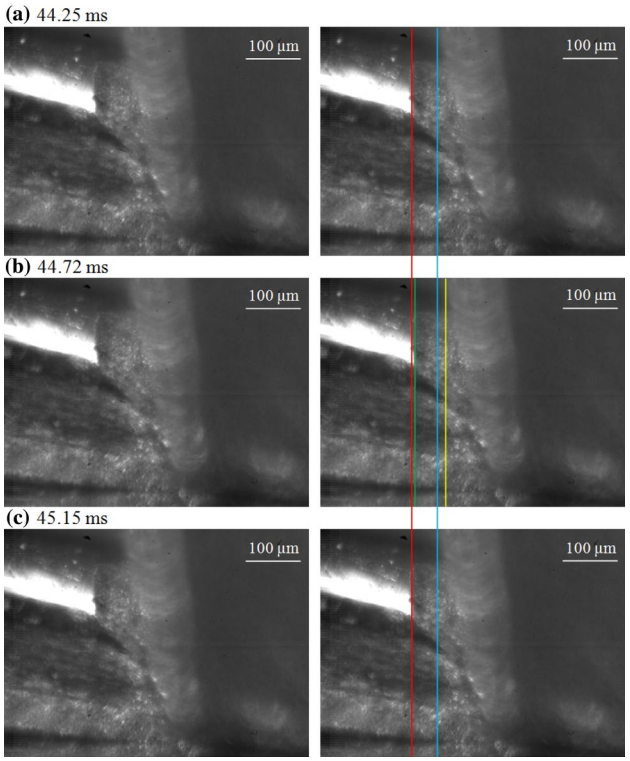

Fig. 6 Vibration induced relative motion under 9 N 17.9 W

observed by the increase of the exposed filet contact region. In addition, the deformation of the wire can be indicated by the change of the vertical position of the tool. As mentioned above, the displacement of the substrate is much smaller than the resolution of the real-time observation system and is thus ignored in this work. Therefore, the moving of the wire can be directly considered as the relative motion between the wire and the substrate.

The vibration induced relative motion is shown in Fig. 6. (a), (c) and (b) show the left-most and the right-most positions of the tool and the wire in an observed vibration cycle, respectively. The peak–peak vibration amplitude of the wire during this period is represented by the red and the green lines and is about 4.4 µm. This can be considered as the vibration induced relative motion amplitude at the w/s interface. The peak–peak vibration amplitude of the tool that is represented by the blue and the yellow lines is about 13.2 µm. Therefore the relative motion amplitude at the w/t interface is about 4.4 µm (zero-peak). The small relative motion amplitude at the w/s interface and the large relative motion amplitude at the w/t interface were caused by the formation of a large amount of microwelds that constrained the motion of the wire in the latter bonding stage.

Since the recording rate was smaller than the bonding frequency, which means that the bonding process was undersampled, the observed vibration cycle was not the vibration

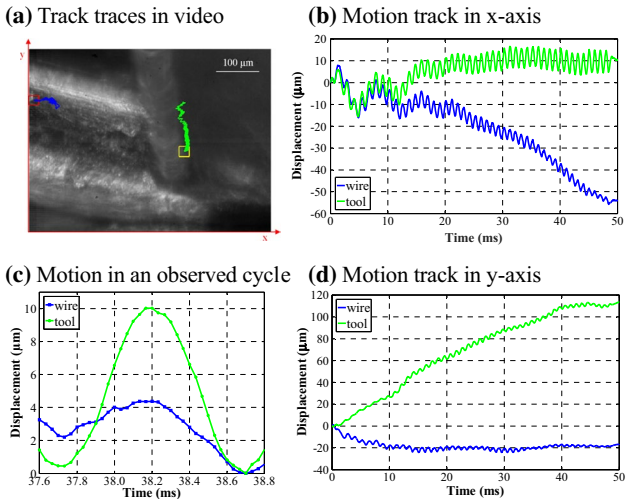

Fig. 7 Motion track of wire and tool under 7.5 N and 17.9 W

cycle in reality. Instead, each observed vibration cycle consists of a number of real vibration cycles depending on the phase difference. In the video shown in Fig. 6, each observed vibration cycle is constituted by ~ 60 US vibration cycles where ~ 30 frames were taken. Despite of the under-sampling rate, the vibration amplitude detected by the video can still reflect the real amplitude due to the small phase difference between successive frames. The values of the vibration amplitude of the tool detected by the videos are also in accordance to the measurements by the laser vibrometer. As a result, the real-time observation is proved to be a powerful tool for the detection of relative motions during bonding processes.

3.2 Motion Track by MATLAB

In this work, the motions of the tool and the wire were tracked by the mean shift method in MATLAB. Mean shift is a non-parametric iterative algorithm that is widely used in computer vision. It combines the coordinate space and the feature space to define and search the target vector in a series of images [25]. In this section, the tracking of the process under 7.5 N 17.9 W is given as an example. As shown in Fig. 7a, the areas as marked by the red and the yellow squares were selected for tracking the motions of the wire and the tool, respectively. The tracked horizontal (x-axis) and vertical (y-axis) displacements of the wire and the tool are correspondingly illustrated in Fig. 7b, d. Since the motion of the wire and the tool in x-axis plays an essential role in the bonding process, the motion in x-axis is mainly discussed in the following sections. It shall be noted again that the cycles in the sinusoids curves are not the US vibration cycles. Each cycle in the curves in Fig. 7 represents ~ 60 US vibration cycles.

The relative motion between the wire and the tool can be easily observed in the motion tracks through the bonding process in Fig. 7b and a single observed vibration cycle in Fig. 7c. In the beginning stage, the equilibrium position of the tool greatly changed, which might be due to the unbalanced stress distribution during the normal force loading. After this period, the change of the equilibrium position became much smaller and negligible. The peak–peak vibration amplitude of the tool is ~ 9.9 μm (see Fig. 7b) which is in accordance to the laser vibrometer measurements. Therefore, the tracked values by the mean shift method are accurate and are able to reflect the peak values of the vibration. The same as the observed situation in Sect. 3.1, the tracking curve clearly shows the two component of the wire displacement—continuous plastic deformation induced displacement and vibration induced displacement. As shown in Fig. 7b, the continuous plastic deformation induced displacement is about 64 μm. The vibration induced displacement amplitude (peak–peak) decreased from 7.6 to 4.0 μm. In other words, the continuous plastic deformation induced relative motion was around 64 μm and the vibration induced relative motion amplitude (peak–peak) increased from 1.3 to 5.9 μm during the bonding process.

Due to the elastic deformation of the wire during the vibration cycles, the vibration induced displacement amplitudes at different heights of the wire are different [26]. Therefore, different areas on the wire were tracked for comparison. As shown in Fig. 8a, a region close to the top of the wire and a region close to the bottom of the wire were selected. The tracking curves in Fig. 8b show no clear difference on the vibration components. This might be due to the resolution of the observation system which is much larger than the elastic deformation induced difference on the vibration amplitudes. On the other hand, the two curves vary a lot on the material flow induced displacements due to the bending up of the wire during the bonding process. To better represent the relative motions, the lower part of the wire as in the yellow square in Fig. 8a is selected so that the influence of the bending of the wire can be eliminated. Since it is made of tungsten carbide with a large stiffness, the bonding tool can be considered as a rigid body. As a result, any part of the tool can be selected as the tracking area.

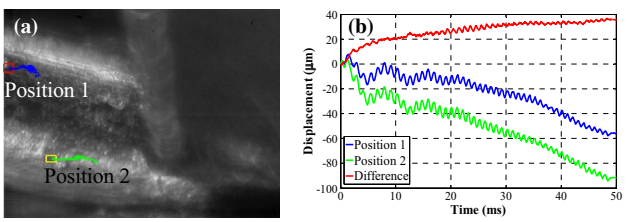

Fig. 8 Comparison the motion at different points on the wire under 7.5N17.9W

3.3 Impact of Parameters on Relative Motions

The current trends and motion tracks for the selected bonding processes under the nine settings in Table 1 are provided in Figs. 9 and 10, respectively. The currents in Fig. 9 indicated the vibration amplitudes of the tool during the bonding processes, which were reflected in the corresponding motion tracks of the tool in Fig. 10.

An obvious feature that can be observed from Fig. 10 is the change of the equilibrium position during the initial bonding stage. It existed in all processes where the change was sometimes ignorable and sometimes significant. When the change of the equilibrium position is significant, the process can be greatly influenced. For example, the process of Fig. 10h had a very large change of the equilibrium in the beginning stage, which might result into an early exposure of a relative large area of metal–metal contact. The vibration amplitude of the wire was thus greatly reduced after this period.

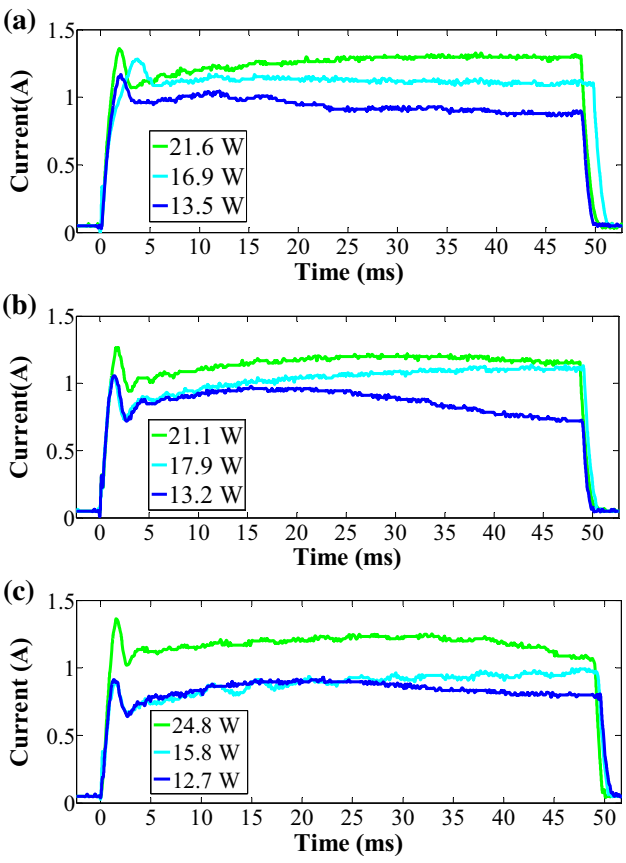

Fig. 9 Current trends of the bonding processes for **a** 6 N, **b** 7.5 N and **c** 9 N

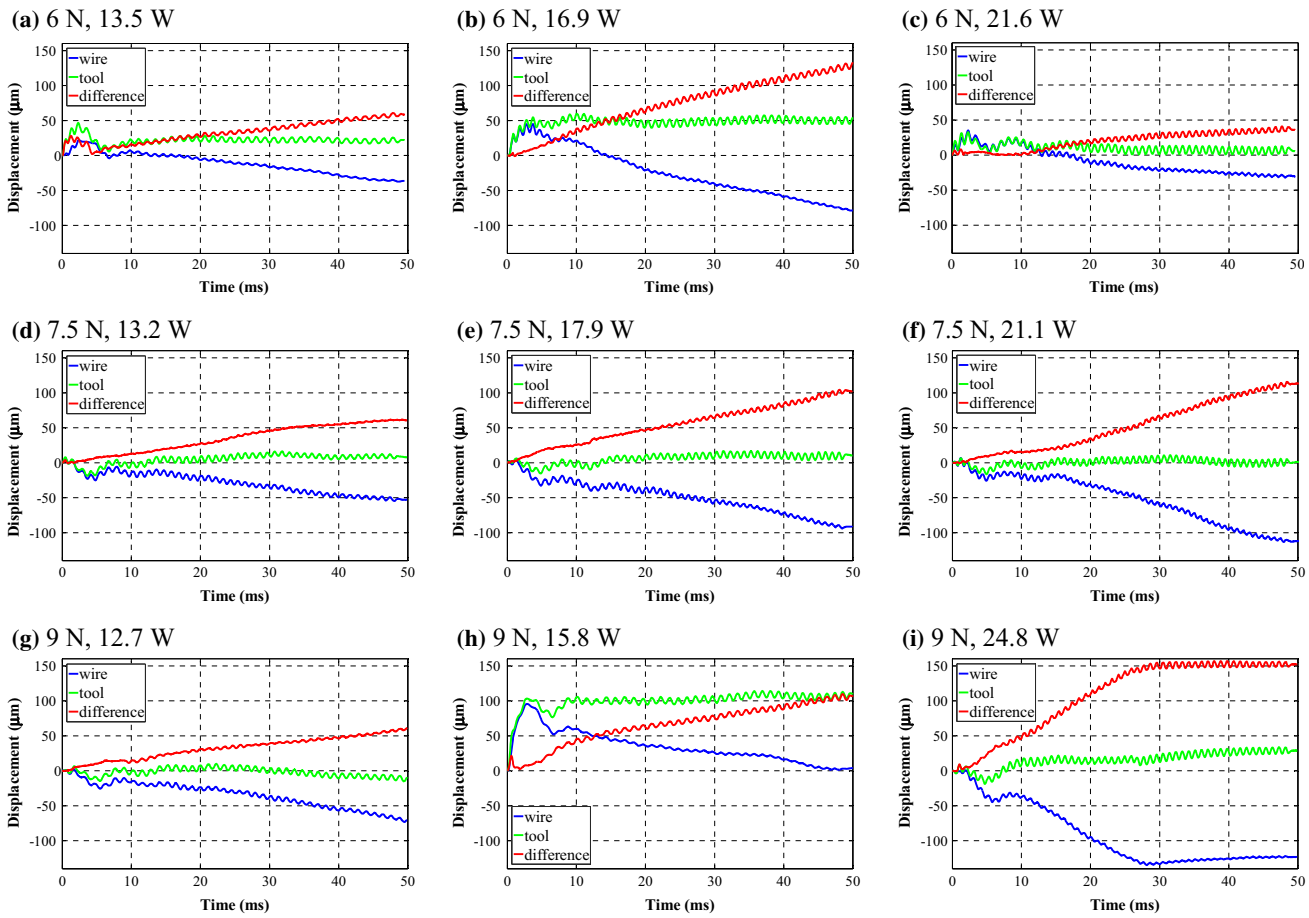

Fig. 10 Motion tracks of the wire and the tool

From Fig. 10, it can be seen that the US power can significantly enhance the continuous plastic deformation induced relative motion except (c). In the case of (c) where a small normal force was coupled with a high US power, however, the plastic deformation of the wire was not enhanced compared to that in (b), which indicates that the normal force was not big enough to transfer such high US power to the wire. With the increase of normal force under the same US power, no obvious change of the continuous plastic deformation induced relative motion was found for low and medium level US power processes. Since larger normal forces caused larger initial plastic deformation during the pre-deformation stage, more energy was required for the processes under larger normal forces to obtain a similar continuous plastic deformation induced relative motion after the larger initial deformation. As the US power increased to high level, a significant increase of the continuous plastic deformation induced relative motion was obtained. In other words, under the current experimental conditions, more US energy can be transferred to the wire by a larger normal force; specifically when a high level US power is applied, a larger continuous plastic deformation induced relative motion can be obtained by loading a larger normal force. These prove that the influences of the normal force and the US power are interdependent.

For all the processes, a clear increase of the vibration induced relative motion at the w/t interface can be observed with the increase of the process time, as shown in the red curves in Fig. 10. Equivalently, the vibration induced relative motion at the w/s decreases as shown by the blue curves. This indicates that microwelds were formed during the process to prevent further vibration of the wire, especially the bottom part of the wire. Since the processes were only controlled by a phase-locked loop and the driving currents were somehow constant, such incremental curves could reflect a good bonding quality. For example, when Fig. 10d is compared to Fig. 10e, there is no obvious increment of the vibration induced relative motion. In addition, the continuous plastic deformation is smaller; under the same normal force, the w/s interface is smaller as well. Therefore, the bonding strength of process (d) is much smaller. The corresponding shear force and interface area of the process in Fig. 10 are shown in Table 2.

Table 2 Shear force (SF) and interface area (IA) of the bonds under the nine settings

Normal Force \ US Power		Low	Medium	High
6 N	*SF (N)*	13.68 ± 1.23	15.25 ± 1.00	14.90 ± 2.11
	IA (μm^2)	290565 ± 49623	306647 ± 27181	291341 ± 49624
7.5 N	*SF (N)*	15.63 ± 2.14	19.73 ± 2.61	17.99 ± 1.64
	IA (μm^2)	320268 ± 46155	336276 ± 23794	357661 ± 22169
9 N	*SF (N)*	18.79 ± 0.60	18.98 ± 2.88	17.11 ± 2.37
	IA (μm^2)	362209 ± 24681	380054 ± 32800	420418 ± 28509

Under the same normal force, an increase of the input US power could enhance the vibration induced relative motion at the w/t interface. Especially when the US power was at a high level, a large normal force is required to avoid serious vibration induced relative motion at the w/t interface. When the power stayed the same, the smallest vibration induced relative motion occurred at 7.5 N and the vibration amplitude of the wire was the largest. The lower level of the normal force was too small to transfer the US energy to vibrate the wire while the higher level of the normal force induced damping was too big to prevent the vibration of the wire. Even though a high power or a large normal force leads to a large interface area, a high shear force is not always generated (see Table 2) as a high power could be detrimental to the already formed microwelds and a large normal force induced high damping is not beneficial for the oxide removal process.

4 Results and Discussion on Energy Flow

4.1 Energy at the Transducer

The transducer converts the supplied electrical energy to mechanical energy while some energy is lost at the transducer. The input electrical energy to the transducer can be calculated as:

$$E_{tran\ input}(t) = \int_0^t u(t)i(t)dt \tag{1}$$

where $u(t)$ and $i(t)$ are the instantaneous voltage and current at the process time t, respectively.

The loss of energy at the transducer is due to the impedance of the transducer whose equivalent electric model is sketched in Fig. 11. "Process" means the impedance within the bonding domain including the wire, the substrate and the two interfaces while it is not the part of the transducer. Since the transducer always runs at its natural frequency, which is confirmed by the phase-locked-loop control, the energy is only consumed at the equivalent resistance R_m.

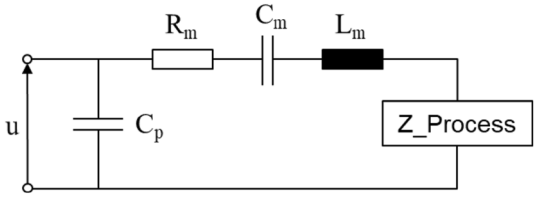

Fig. 11 An equivalent electric model of the transducer

The resistance of the used transducer was measured to be 14.45 Ω. The consumed energy can be calculated as:

$$E_{tran\ loss}(t) = \int_0^t R_m i^2(t)dt \tag{2}$$

Some energies are stored and exchanged between L_m and C_m for oscillating the transducer and the tool. They are calculated as:

$$E_{storage}(t) = \frac{1}{2}L_m i^2 t + \frac{1}{2}\frac{q^2(t)}{C_m}. \tag{3}$$

4.2 Energy at the Voice Coil Actuator

The same as the transducer, some energy is also lost at the VCA. Since VCA is supplied by a DC power, the coils can be simply considered as a resistor R_{VCA} (measured to be 20.09 Ω). The consumed energy is calculated as:

$$E_{VCA\ loss}(t) = \int_0^t R_{VCA} i^2(t)dt \tag{4}$$

The output energy of VCA is equal to the work it conducts during the bonding process:

$$E_{VCA\ output} = W_{NF}(t) = F_N S_N(t) \tag{5}$$

where F_N is the normal force generated by VCA which is constant during the process; $S_N(t)$ is the vertical displacement of the tool tip at the process time t and is derived from the motion tracking in y-axis, like Fig. 7d.

4.3 Friction Energy Due to Vibration

As described in Sect. 3, the relative motions at the w/t interface and the w/s interface are caused by the US vibration and the continuous plastic deformation. The friction energy can be thus divided into two parts—the friction energy due to vibration and the friction energy due to plastic deformation. The first part can be calculated by Coulomb's Law as in the following equations:

$$E_{vfriction,w/t}(t) = \int_0^t \mu_{w/t} F_N(t) d\left[D_{v,w/t}(t)\right] \quad (6)$$

$$E_{vfriction,w/s}(t) = \int_0^t \mu_{w/s}[1-\varphi(t)] F_N(t) d\left[D_{v,w/s}(t)\right] \quad (7)$$

where $D_v(t)$ is the distance accumulated by the vibration induced relative motion at the corresponding interface at the process time t; μ is the dynamic friction coefficient for the corresponding sliding contact and is obtained from literature; $\varphi(t)$ is the cleaning coefficient at the process time t. As mentioned before, the vibration induced relative motion amplitude at the w/s interface is directly considered to be the vibration amplitude of the wire.

The friction coefficient between the tool and the wire $\mu_{w/t}$ was measured to be 0.9151 ± 0.0979. The wire-substrate contact before the exposure of pure metal contact can be considered as alumina–alumina contact since both the wire and substrate surfaces are covered by alumina. According to Blau, the friction coefficient $\mu_{w/s}$ is taken as 0.41 [27].

A cleaning coefficient is introduced to distinguish the oxide-free (or metal–metal contact) area and the area where oxides retain. It is considered as the ratio of the oxide-free area over the whole interface. The oxide-free area can be indicated by microwelds area as microwelds are formed after the direct metal–metal contact. Based on the contact resistance measurements by Seppänen et al., it was stated that the first microweld forms within 2–5 ms depending on the process parameters and the microwelds area increased linearly during the bonding process [28]. In this work, the first microweld is considered to form at 3.5 ms for all processes and the cleaning coefficient increases linearly to a final value at 50 ms, as shown in Fig. 12b. The final values of the cleaning coefficient for the nine processes were estimated according to Table 2. First, a reference interface that was fully covered by microwelds shall be selected. This was carried out by the comparison of the microwelds shear stress. By dividing the shear force over the corresponding interface area, the 7.5 N 17.9 W specimen received the largest

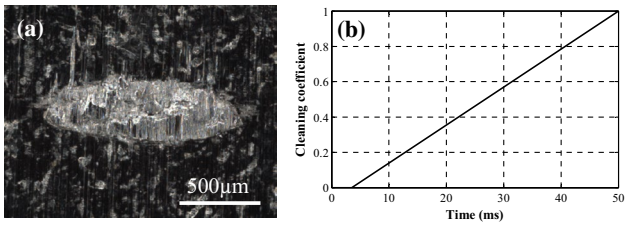

Fig. 12 **a** The final interface, **b** cleaning coefficient of the process under 7.5 N 17.9 W

Table 3 Final cleaning coefficient under different parameter settings

Normal Force \ US Power	Low	Medium	High
6 N	0.8075	0.8530	0.8768
7.5 N	0.8370	1.0000	0.8626
9 N	0.8195	0.8566	0.6873

value—58.31 MPa. This value is a little larger than the ultimate shear stress of 99.999% aluminum [29]. The reason can be attributed to the change of dislocation density and the recrystallization process. This value is thus considered as the ultimate shear stress of microwelds. In addition, wire residues (see Fig. 12a) can be observed on the whole w/s interface after the shear test. As a result, the final cleaning coefficient for the 7.5 N 17.9 W process is set as 1.0. The final cleaning coefficients for the other processes can be then calculated and shown in Table 3.

From Table 3, it can be seen that a larger force or a higher US power does not mean a higher cleaning coefficient. For example, under 9 N 24.8 W, the cleaning coefficient is much smaller than those under the other settings. This indicates that a high US power combined with a large force could damage the existing microwelds and prevent the formation of new microwelds. On the other hand, when the cleaning coefficients are similar, the process under a larger normal force obtains a larger oxide-free area. Take the 6 N 13.5 W and 9 N 12.7 W processes as an example, due to the larger normal force, the latter process had a larger w/s interface which resulted into a larger oxide-free area despite the similar value of the cleaning coefficient as that of the former process.

Since the processes were optically observed, only the visible part of the wire where the tool did not contact was selected for analyzing the relative motion behavior. According to Long et al., the vibration induced relative motion amplitude at this visible part (the same as that at the end of the w/t contact) is larger than that at the invisible part [12]. As a result, the tracked amplitude shall be larger than the average value in reality and the calculated energy is thus higher than the energy consumption in reality.

4.4 Friction Energy Due to Plastic Deformation

The plastic deformation induced friction energy is shown below:

$$E_{pfriction,w/t}(t) = \int_0^t \mu_{w/t} F_N d\frac{S_{p,w/t}(t)}{2} \quad (8)$$

$$E_{p\,friction,\,w/s}(t) = \int_0^t \mu_{w/s}(1-\varphi(t))F_N d\frac{S_{p,w/s}(t)}{2} \tag{9}$$

where $S_p(t)$ is the plastic deformation induced relative motion displacement at the corresponding interface at the process time t. The plastic deformation induced displacements vary at different parts of the wire. And the longer distance from the center of wire is, the larger the displacement is. Since the tracked region located at the visible part that is out of the contact with the tool, it resulted in the largest relative motion displacement induced by the plastic deformation. If the wire keeps at its equilibrium place, the center point has no relative motion. Therefore, half of the relative motion displacement at the detected region is considered as the average relative motion displacement of the whole wire.

4.5 Kinetic Energy

The kinetic energy of the wire is provided by the US energy:

$$E_{v,\,wire}(t) = \int_0^t \frac{1}{2} md\left[v_w^2(t)\right] \tag{10}$$

where m is the mass of the wire underneath the tool tip and is calculated to be ~ 0.379 mg; $v_w(t)$ is the vibration speed of the wire at the process time t.

4.6 APE Energy

The bulk deformation of the wire is caused by the normal force and the vibration induced APE effect. Therefore, the energy for the bulk deformation of the wire comes from two parts—the work of the normal force and the US energy for APE. The work of the normal force used for the wire deformation is:

$$E_{NF\,defor,\,wire}(t) = W_{NF}(t) - E_{p\,friction,\,w/s}(t) - E_{p\,friction\,w/t}(t) - E_{pmw}(t) \tag{11}$$

The APE energy, however, is currently unable to be theoretically calculated as the mechanism is still unknown. In this work, an equivalent work to deform the wire is used for an estimation of the APE energy. It is calculated as:

$$W_{defor,\,wire}(t) = \int_0^t F_{add,N}(t)d\left[S_N(t)\right] - E_{add\,p\,friction,\,w/s}(t) - E_{addpfriction,w/t}(t) \tag{12}$$

$$E_{add\,p\,friction,\,w/t}(t) = \int_0^t \mu_{w/t}F_{add,N}(t)d\frac{S_{p,w/t}(t)}{2} \tag{13}$$

$$E_{add\,p\,friction,\,w/s}(t) = \int_0^t \mu_{w/s}F_{add,N}(t)d\frac{S_{p,w/s}(t)}{2} \tag{14}$$

where $F_{add,N}(t)$ is the additional normal force required to deform the wire to the vertical displacement $S_N(t)$ when no US energy is applied; since the additional large normal force will also cause additional friction, the additional friction energy $E_{add\,p,\,friction}(t)$ shall be eliminated.

As the bulk deformation of the wire has two energy sources, the equivalent work can also be expressed by:

$$W_{defor,\,wire}(t) = E_{NF\,defor,\,wire}(t) + E_{APE}(t) \tag{15}$$

The APE energy can be thus calculated as:

$$E_{APE}(t) = W_{defor,\,wire}(t) - E_{NF\,defor,\,wire}(t) \tag{16}$$

4.7 Microwelds Formation and Breakage

During the bonding process, the formation, deformation and breakage of microwelds coexist. In order to estimate the required energy for these changes, as inspired by Gaul et al. [29], the changes of the microwelds are considered as friction at the w/s interface within the oxide-free area. Since both the vibration and the plastic deformation induced relative motions can cause these changes, the equivalent friction energy is divided into two parts as:

$$E_{v\,mw}(t) = \int_0^t \mu_{mw}\varphi(t)F_N(t)d\left[D_{v,w/s}(t)\right] \tag{17}$$

$$E_{p\,mw}(t) = \int_0^t \mu_{mw}\varphi(t)F_N(t)d\left[S_{p,w/s}(t)\right] \tag{18}$$

where μ_{mw} is the friction coefficient for microwelds formation, deformation and breakage. This equivalent coefficient must be larger than the friction coefficient of Al–Al contact which is the initiation of microwelds formation, and smaller than the equivalent value by which all microwelds are broken. Referred from the literature, the friction coefficient for Al–Al contact is taken as 0.865 [27, 30]. Since the whole interface of the 7.5 N 17.9 W specimen was bonded, the equivalent friction coefficient for breaking all microwelds is calculated to be 2.63. Finally, the average value of the coefficients under these two extreme conditions 1.748 is taken as μ_{mw}.

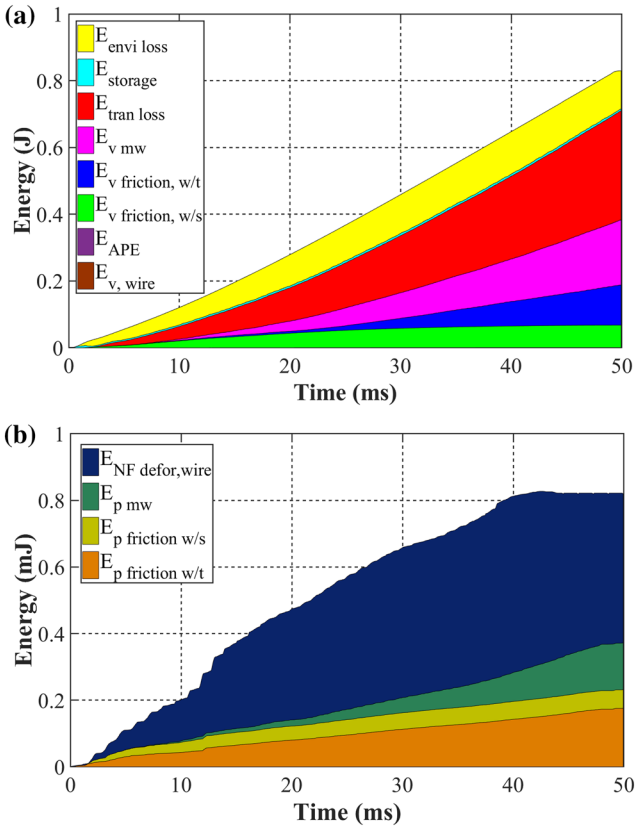

Fig. 13 Energy flow from **a** transducer, **b** VCA through the bonding process under 7.5 N 17.9 W

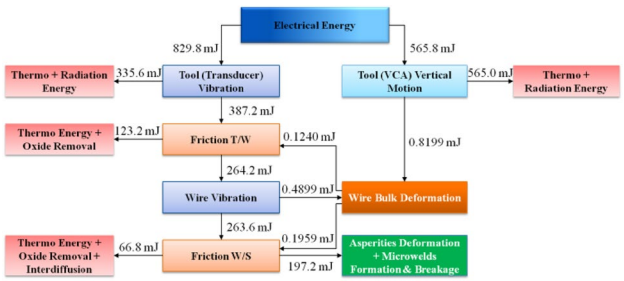

Fig. 14 Quantification of the energy flow at the process time of 50 ms under 7.5 N 17.9 W

4.8 Energy Emitted to the Environment

Apart from the above calculated energies, some US energy is emitted to the environment including the substrate, the non-contacted part of the wire and the ambient space. It can be calculated by subtracting the sum of the energies mentioned above (except the energy at VCA) from the total input energy of the transducer. On the other hand, this part contains errors as well since the above calculations are based on many assumptions and approximations. Due to some approximations which are larger than the values in reality, the subtraction may result in a negative value.

4.9 Energy Flow under 7.5 N 17.9 W

All the above mentioned energies are calculated for the 7.5 N 17.9 W process and the energy flows from the US transducer side are shown in Fig. 13a. The energy flows from VCA are shown in Fig. 13b. By picking up the values at the process time of 50 ms, the proposed flow chart in Fig. 2 is quantified as in Fig. 14. Due to the resistance, a large amount of energy was dissipated at the transducer even though it was always controlled in resonance. Finally, 335.6 mJ out of 829.8 mJ was lost at the transducer while 59.56% of the total energy was transferred to the bonding domain and the environment.

It is obvious that the majority of the output energy from the transducer was consumed by the vibration induced friction at the w/s interface, the vibration induced friction at the w/t interface and the vibration induced microwelds formation, deformation and breakage. As more and more microwelds were formed to constrain the vibration induced relative motion at the w/s interface, less and less energy was accumulated for the friction and the energy curve becomes flat at the latter bonding stage. On the other hand, since only ignorable microwelds were formed and broken at the w/t interface and the relative motion became larger and larger, the friction at this interface was not weakened and the energy curve as well as its slope keeps increasing. In addition, the friction coefficient at the w/s interface is much smaller than that at the w/t interface. As a result, the vibration induced friction at the w/s interface (66.7 mJ) cost much less energy than the vibration induced friction at the w/t interface (123.0 mJ). Under this parameter settings (7.5 N 17.9 W), a comparably large part of US energy (23.75%) flew to the w/s interface for microwelds formation, deformation and breakage. The high shear strength indicates that more energy was used for formation rather than breakage. Therefore, the incremental curve can be simply considered as a formation curve.

Only 0.4899 mJ of the US energy was spent for APE and the kinetic energy of the wire was 0.0577 mJ. These small values make the two energy areas invisible in Fig. 13a. The deduced APE energy is 4.95 times higher than the work (0.0990 mJ) the normal force conducted during the pre-deformation stage, which is reasonable to explain the existence of the continuous plastic deformation. In addition, this value is close to the deformation energy provided by VCA (0.5000 mJ) and can explain the 40–50% reduction of the yield stress [19]. The small kinetic energy is due to the small mass of the wire. The rest US energy was emitted to the ambient environment.

Compared to the items caused by vibration, only a little amount of energy was allocated to the items induced

by plastic deformation and the difference is in the order of three. This is easy to understand with the comparison of the total distances. Even in the case where the average vibration induced relative motion amplitude is only 1 μm, the relative motion totally accumulates a 12 m distance as a 50 ms of 60 kHz vibraton contains 3000 vibration cycles. In contrast, the maximum plastic deformation induced relative motion is only ~ 150 μm (see Fig. 10). The changes of these energies are shown in Fig. 13b. As the plastic deformation continued throughout the whole bonding process, the energy curves for the deformation induced friction at the two interfaces and the microwelds formation and breakage at the w/s interface keep increasing. Despite of the small value of $E_{p\ friction\ w/s}$, this energy is essential for expanding the w/s contact area which is a prerequisite for the formation of large amounts of microwelds. During the last ~ 8 ms of the bonding process, the tracking results show that the tool stopped moving downwards while the tracked wire part continued to move horizontally. This greatly enlarges $E_{add\ p\ friction}$ and $E_{p\ mw}$ and leads to an unexpected downwards bending of the $E_{NF\ defor,\ wire}$ energy curve. As can be seen from the small value (0.1404 mJ) of plastic deformation induced microwelds formation, deformation and breakage, the vibration induced relative motion is mainly responsible for the formation of microwelds.

Due to the large resistance of the coils of VCA, 99.9% of the input energy to VCA was directly consumed at VCA. Nevertheless, the small amount of the output energy is significant to the bonding process. Without the coupling of the tool, the wire and the substrate by these output energies, no US energy can be transferred to the wire and the w/s interfaces.

4.10 Impact of Parameters on Energy Flows

Under different parameter settings, the energy flows significantly differ. To exhibit the differences, the energy flows from the US transducer side under the other parameter settings are calculated and shown in Fig. 15.

As mentioned before, since the tracked relative motions are larger than the average values in reality, the sum of the calculated energies could exceed the input energy to the transducer which is normally the uppermost line but the dash line in Fig. 15h. Nevertheless, the input value of (h) is only exceeded by 2.59% which is in an acceptable range. From this point of view, the calculations of the energy flows do not significantly deviate from the energy consumptions in reality.

Naturally, the larger the US power (or current) was applied, the more energy was consumed at the transducer due to the equivalent resistance. $E_{v\ friction,\ w/t}$ is increased by applying a larger US power but also affected by the change of the equilibrium position of the tool. For example, in the case of 9 N 15.8 W, this energy consumption is not lower than that of 9 N 24.8 W as the bottom surface of the wire was constrained at an early stage. A medium force can more efficiently transfer US energy to the wire and the w/s interface while more energy was emitted to the environment when a small normal force was coupled with a large power (e.g. 6 N 21.6 W).

The influences of the process parameters on $E_{v\ friction,\ w/s}$ and $E_{v\ mw}$ are complex as these energy flows are also significantly influenced by the cleaning coefficient and the change of the equilibrium position. A high cleaning coefficient can significantly decrease $E_{v\ friction,\ w/s}$, e.g. the $E_{v\ friction,\ w/s}$ of 7.5 N 17.9 W is even a little smaller than that of 7.5 N 13.2 W. A low cleaning coefficient (e.g. 9 N 24.8 W) greatly increases $E_{v\ friction,\ w/s}$. If a great change of the equilibrium position exists in the beginning stage, the resulted $E_{v\ friction,\ w/s}$ is greatly reduced (e.g. 9 N 15.8 W). A small force can only transfer limited energy to $E_{v\ mw}$ for microwelds formation, deformation and breakage while an increase of the normal force can significantly enhance $E_{v\ mw}$. If the US power is well coupled with the normal force, more energy can be applied for microwelds formation. When the two factors are not well coupled, even $E_{v\ mw}$ can be increased by increasing the US power, the energy flowing to microwelds formation does not necessarily increase. Instead, more microwelds will be broken. As expected, a large cleaning coefficient (or an effective oxide removal process) leads to a larger $E_{v\ mw}$ and the energy for the formation of microwelds increases as well.

The impacts of the normal force and US power on the loss and output energies at VCA are shown in Table 4. Since the process time was the same for all the nine processes, the energy consumption at VCA was only influenced by the normal force (applied current at VCA). With regard to the work VCA conducted during the processes, in general, the increase of either the normal force or the US power enhanced the output energy of VCA. The only exception is 6 N 21.6 W where not enough energy was delivered to the wire for bulk deformation. As the plastic deformation got smaller than the other processes, the work conducted by VCA decreased.

5 Conclusions

Based on real-time observations, the impacts of process parameters on the relative motion behaviors at the wire/substrate and the wire/tool interfaces during US wire bonding process were quantitatively investigated. The relative motions were proved to be induced by both continuous plastic deformation and US vibration. The motion traces of the tool and the wire were tracked and the results showed that

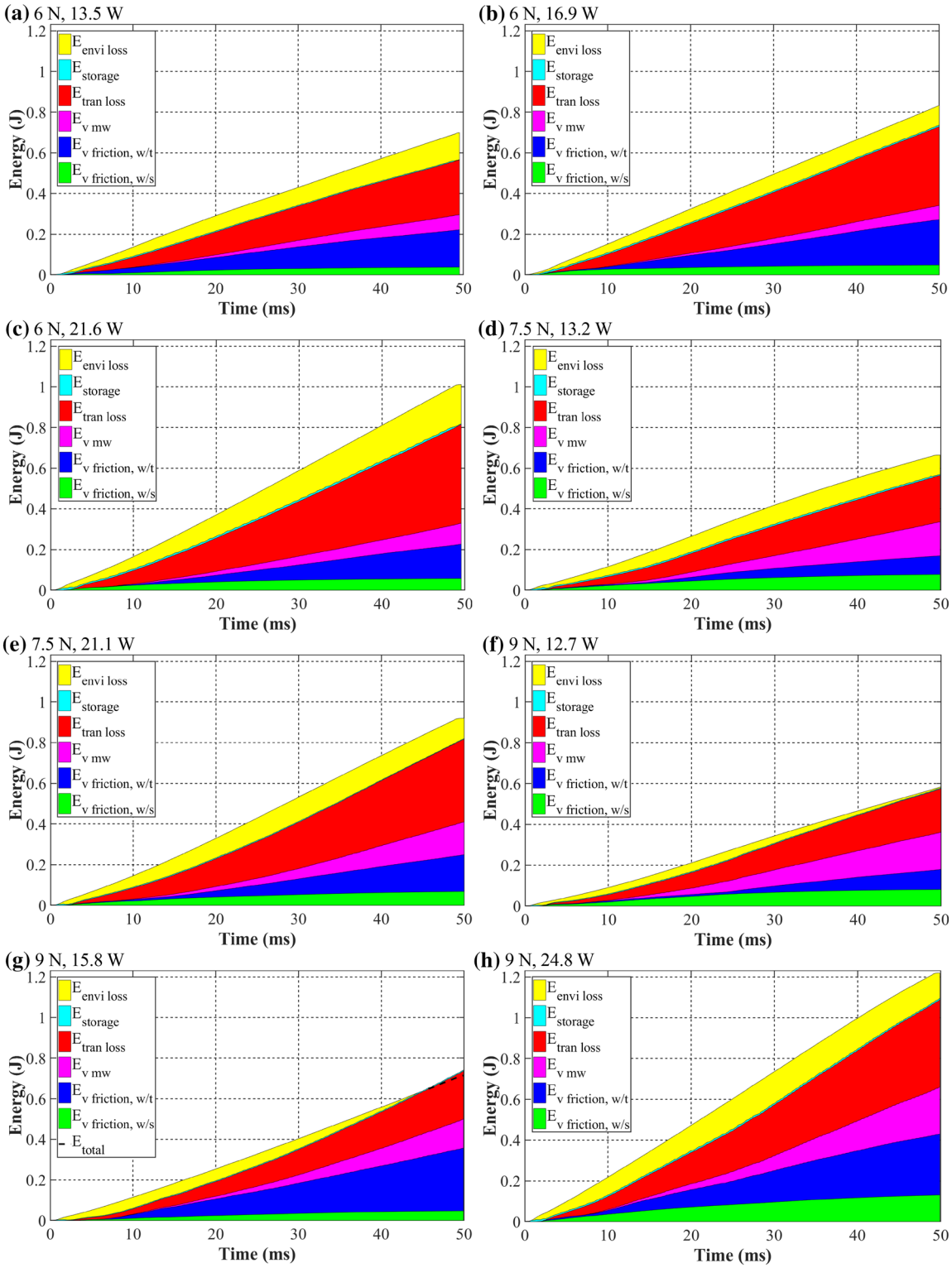

Fig. 15 Energy flow from the transducer during the other processes

Table 4 Loss and output energies at the voice coil actuator under different parameter settings

Normal Force \ US Power		Low	Medium	High
6 N	$E_{VCA\,loss}$ (mJ)	361.62	361.62	361.62
	$E_{VCA\,output}$ (mJ)	0.7265	0.7367	0.6697
7.5 N	$E_{VCA\,loss}$ (mJ)	565.03	565.03	565.03
	$E_{VCA\,output}$ (mJ)	0.7991	0.8199	0.8575
9 N	$E_{VCA\,loss}$ (mJ)	813.65	813.65	813.65
	$E_{VCA\,output}$ (mJ)	0.9147	1.3324	1.4699

the impacts of the normal force and the US power are interdependent. A middle level of normal force and US power can be well coupled, which leads to enough vibration at the wire/substrate interface and an increasing vibration induced relative motion amplitude at the wire/tool interface. An energy flow model was further quantified according to the detected relative motions. The majority of the US energy flows to the vibration induced friction at the wire/substrate and the wire/tool interfaces, and the vibration induced microwelds formation, deformation and breakage. Even though the rest items are significant to the process, only a little amount of energy is delivered to them. A good coupling of the normal force and the US power could guide more energy to the wire/substrate interface for microwelds formation. If the two factors are not well coupled, even though more energy can be provided to the wire/substrate interface, the breakage of microwelds will take up a big part. Other than the process parameters, a big change of the equilibrium position of the tool in the beginning stage could significantly alter the energy flows.

Acknowledgements We gratefully acknowledge the support from the Ministry of Science and Culture of Lower Saxony, Germany within the Multifunktionale Aktive und Reaktive Interfaces und Oberflächen (MARIO) program and Deutsche Forschungsgemeinschaft (DFG) program (TW75/8-1|WA564/40-1). Great thanks to Hesse Mechantronics GmbH for providing the bonding head HBK05 and Mr. Heiner Ramsbott from Vision Research Europe for providing the lens.

References

1. Harman, G. G. (2010). *"Wire bonding in microelectronics* (3rd ed.). New York City: McGraw-Hill.
2. Ali, S., Hian, S., & Ang, B. (2014). The effects of wire geometry and wire layout on wire sweep performance using LQFP packages in transfer mold. *International Journal of Precision Engineering and Manufacturing, 15*(9), 1793–1799.
3. Harthoorn, J.L., "Ultrasonic metal welding," Doctoral dissertation, Technical University of Braunschweig, 1978.
4. Long, Y., Twiefel, J., & Wallaschek, J. (2017). A review on the mechanisms of ultrasonic wedge-wedge bonding. *Journal of Materials Processing Technology, 245,* 241–258.
5. Uthe, P. M. (1969). Variables affecting weld quality in ultrasonic aluminum wire bonding. *Solid State Technol., 5,* 72–77.
6. Joshi, K. C. (1971). The formation of ultrasonic bonds between metals. *Welding Journal, 50*(12), 840–848.
7. Winchell, V. H. I. I., & Berg, H. (1978). Enhancing ultrasonic bond development. *IEEE Transactions on Components, Hybrids, and Manufacturing Technology, 1*(3), 211–219.
8. Osterwald, F., "Verbindungsbildung beim UltraschallDrahtbonden: Einfluß der Schwingungsparameter und Modellvor-stellungen," Dissertation, Technical University of Berlin, 1999.
9. Gaul, H., Schneider-Ramelow, M., & Reichl, H. (2009). Analysis of the friction processes in ultrasonic wedge/wedge-bonding. *Microsystem Technologies, 15*(5), 771–775.
10. Mayer, M., Schwizer, J., Paul, O., Bolliger, D., & Baltes, H. (1999). In situ ultrasonic stress measurements during ball bonding using integrated piezoresistive microsensors. In *The Pacific Rim/ASME International Intersociety Electronic & Photonic Packaging Conference, Hawaii, USA*, pp. 973–978.
11. Gaul, H., Schneider-Ramelow, M., & Reichl, H. (2007). Hochgeschwindigkeitsaufnahmen der Werkzeug-und Drahtschwingung beim US-Wedge/Wedge-Bonden. *Produktion von Leiterplatten und Systemen H, 8,* 1529–1534.
12. Long, Y., Dencker, F., Wurz, M., Feldhoff, A., & Twiefel, J. (2016). A deeper understanding on the motion behaviors of wire during ultrasonic wedge-wedge bonding process. In: International symposium on microelectronics, Pasadena, USA, pp. 427–432.
13. Long, Y., Dencker, F., Schneider, F., Emde, B., Li, C., Hermsdorf, J., Wurz, M., & Twiefel, J. (2016). Investigations on the oxide removal mechanism during ultrasonic wedge-wedge bonding process. In Electronics *packaging technology conference*, Singapore, pp. 405–410.
14. Xu, T., Walker, T., Chen, R., Fu, J., & Luechinger, C. (2014) Advanced interconnect equipment and process development. In *Electronics packaging technology conference*, Singapore, pp. 564–569.
15. Long, Y., Twiefel, J., Roth, J., & Wallaschek, J. (2015). Real-time observation of interface relative motion during ultrasonic wedge-wedge bonding process. In *International symposium on microelectronics*, Orlando, USA, pp. 419–424.
16. Xu, T., Walker, T., Chen, R., Fu, J., & Luechinger, C. (2015). Bond tool life improvement for large copper wire bonding. In *Electronics packaging and technology conference*, Singapore, pp. 1–5.
17. Unger, A., Sextro, W., Meyer, T., Eichwald, P., Althoff, S., Eacock, F., Hunstig, M., & Guth, K. (2015). Modeling of the stick-slip effect in heavy copper wire bonding to determine and reduce tool wear. In: Electronics packaging and technology conference, Singapore, pp. 1–4.
18. Long, Y., Dencker, F., Isaak, A., Hermsdorf, J., Wurz, M., & Twiefel, J. (2018). Self-cleaning mechanisms in ultrasonic bonding of Al wire. *Journal of Materials Processing Technology, 258,* pp. 58–66.
19. Blaha, F., & Langenecker, B. (1955). Dehnung von Zink-Kristallen unter Ultraschalleinwirkung. *Naturwissenschaften, 42*(20), 556.
20. Blaha, F., & Langenecker, B. (1959). Plastizitätsuntersuchungen von Metallkristallen in Ultraschallfeld. *Acta Metallurgica, 7*(2), 93–100.
21. Murali, S., Srikanth, N., Wong, Y. M., & Vath, C. J. (2007). Fundamentals of thermosonic copper wire bonding in microelectronics packaging. *Journal of Materials Science, 42*(2), 615–623.
22. Maeda, M., Yamane, K., Matsusaka, S., & Takahashi, Y. (2009). Relation between vibration of wedge-tool and adhesion of wire

to substrate during ultrasonic bonding. *Quarterly Journal of the Japan Welding Society, 27*(2), 200s–203s.
23. Long, Y., Dencker, F., Isaak, A., Li, C., Schneider, F., Hermsdorf, J., Wurz, M., Twiefel, J. & Wallaschek, J. (2018). Revealing of ultrasonic wire bonding mechanisms via metal-glass bonding. *Materials Science and Engineering: B, 236,* pp. 189–196.
24. Ille, I., & Twiefel, J. (2015). Model-based feedback control of an ultrasonic transducer for ultrasonic assisted turning using a novel digital controller. *Physics Procedia, 70,* 63–67.
25. Comaniciu, D., & Meer, P. (2002). Mean shift: A robust approach toward feature space analysis. *IEEE Transactions on Pattern Analysis and Machine Intelligence, 24*(5), 603–619.
26. Gaul, H., Schneider-Ramelow, M., Lang, K. D., & Reichl, H. (2006). Predicting the shear strength of a wire bond using laser vibration measurements. *Electronics System integration Technology Conference, Dresden, Germany, 2,* 719–725.
27. Blau, P.J., "Friction Science and Technology," CRC Press. 1995.
28. Seppänen, H., Kurppa, R., Meriläinen, A., & Hæggström, E. (2013). Real time contact resistance measurement to determine when microwelds start to form during ultrasonic wire bonding. *Microelectronic Engineering, 104,* 114–119.
29. Gaul, H., Schneider-Ramelow, M., & Reichl, H. (2010). Analytic model verification of the interfacial friction power in Al us w/w bonding on Au pads. *IEEE Transactions on Components and Packaging Technologies, 33*(3), 607–613.
30. Antle, W. (1964). Friction technique for optimum thermocompression bonds. *IEEE Transactions on Component Parts, 11*(4), 25–29.

Yangyang Long is a research assistant at the Institute of Dynamics and Vibration Research, Leibniz Universität Hannover. His research interests include ultrasonic bonding and welding, ultrasonic assisted metal forming and remanufacturing.

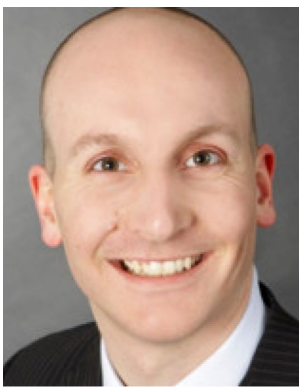

Friedrich Schneider is a research assistatn at Laser Zentrum hannover e.V. He is interested in laser machining.

Chun Li is a master student in the Faculty for Mechanical Engineering, Leibniz Universität Hannover. His research interests include wire bonding and imaging processing.

Jörg Hermsdorf heads the Materials and Processes Department at Laser Zentrum hannover e.V. His research interests include laser-assisted arc light processes, wire deposition welding, laser microwelding of aluminum and copper using solid-state and diode lasers, underwater use of laser system technology and process control for quality assurance with laser processes.

Jens Twiefel heads the research laboratory for piezoelectric and ultrasonic technology at the Institute of Dynamics and Vibration Research at Leibniz Universität Hannover. His research focuses on the adaptation of high-performance ultrasonic technology to new applications and the improvement of the fundamental understanding of the influence of ultrasound on various production processes.

Jörg Wallaschek is Professor and head of the Institute of Dynamics and Vibration Research at Leibniz Universität Hannover. His research interests include Vibration Control Technology and machine dynamics Actuators, piezoelectric and ultrasonic technology, Mechatronics and automotive lighting, Contact mechanics and elastomer friction, and Methodology of scientific work and product development.